

# Center-to-limb observations of the Sun with ALMA

## Implications for solar atmospheric models

C. E. Alissandrakis (Κ. Ε. Αλυσσανδράκης)<sup>1</sup>, S. Patsourakos (Σ. Πατσουράκος)<sup>1</sup>,  
A. Nindos (Α. Νίντος)<sup>1</sup>, and T. S. Bastian<sup>2</sup>

<sup>1</sup> Department of Physics, University of Ioannina, 45110 Ioannina, Greece  
e-mail: calissan@cc.uoi.gr

<sup>2</sup> National Radio Astronomy Observatory (NRAO), 520 Edgemont Road, Charlottesville, VA 22903, USA

Received 7 April 2017 / Accepted 24 May 2017

### ABSTRACT

**Aims.** We seek to derive information on the temperature structure of the solar chromosphere and compare these results with existing models.

**Methods.** We measured the center-to-limb variation of the brightness temperature,  $T_b$ , from ALMA full-disk images at two frequencies and inverted the solution of the transfer equation to obtain the electron temperature,  $T_e$  as a function of optical depth,  $\tau$ .

**Results.** The ALMA images are very similar to AIA images at 1600 Å. The brightness temperature at the center of the disk is 6180 and 7250 K at 239 and 100 GHz, respectively, with dispersions of 100 and 170 K. Plage regions stand out clearly in the 239/100 GHz intensity ratio, while faculae and filament lanes do not. The solar disk radius, reduced to 1 AU, is  $961.1 \pm 2.5''$  and  $964.1 \pm 4.5''$  at 239 and 100 GHz, respectively. A slight but statistically significant limb brightening is observed at both frequencies.

**Conclusions.** The inversion of the center-to-limb curves shows that  $T_e$  varies linearly with the logarithm of optical depth for  $0.34 < \tau_{100\text{ GHz}} < 12$ , with a slope  $dT_e/d\ln \tau = -608$  K. Our results are 5% lower than predicted by the average quiet Sun model C of Fontenla et al. (1993, ApJ, 406, 319), but do not confirm previous reports that the mm- $\lambda$  solar spectrum is better fitted with models of the cell interior.

**Key words.** Sun: radio radiation – Sun: atmosphere – Sun: chromosphere

## 1. Introduction

The solar atmosphere can be probed by measuring the specific intensity of the radiation either as a function of position from the center of the disk to the limb and/or as a function of frequency at the center of the solar disk. Such observations allow, in principle, the inversion of the formal solution of the transfer equation and retrieve the source function of the radiation as a function of optical depth, which is the basis for the computation of empirical atmospheric models.

An important difficulty in this procedure is the complex dependence of the absorption coefficient on the physical conditions and the departures from local thermodynamic equilibrium (LTE) in optical and UV wavelengths. The situation is better in the radio range, which probes the solar atmosphere from the chromosphere to the corona, thanks to the Rayleigh-Jeans approximation to the Planck function and the fact that the quiet Sun emission originates from thermal bremsstrahlung in LTE (see Shibasaki et al. 2011; and Wedemeyer et al. 2016, for details). In this context, observations at millimeter wavelengths provide a valuable tool for atmospheric modeling.

There is a long tradition of such observations with single-dish telescopes, but most of these suffered from low sensitivity and low spatial resolution; for typical dish sizes in the range of 10–15 m the resulting resolution is on the order  $1'$  at  $\lambda = 3$  mm (see Loukitcheva et al. 2004, and references therein). The resolution is improved either by observing at shorter wavelengths (e.g., observations at 0.85 mm reported by Bastian et al. 1993;

and Lindsey et al. 1995, had a resolution of  $\sim 20''$ ) or with larger telescopes, for example, the Nobeyama 45 m telescope, which yields a resolution of  $\sim 20''$  at  $\lambda = 3$  mm (see Irimajiri et al. 1995). Furthermore, during solar eclipses, the edge of the Moon has been used to gain high resolution in one dimension (e.g., Belkora et al. 1992; Ewell et al. 1993). The reported brightness temperatures as a function of frequency show a large scatter due to inherent difficulties in the measurements and possible solar cycle effects.

According to empirical models the mm- $\lambda$  radiation comes mainly from the chromosphere. The Avrett & Loeser (2008) model predicts that most of the emission at 3 cm and shorter wavelengths originates below the transition region (TR), with a small contribution from this region and practically no contribution from the corona. An important issue is that the observations are better fitted with models that represent the cell interior (e.g., Landi & Chiuderi Drago 2003; Loukitcheva et al. 2004) rather than with average models, which predict too much radio flux. Moreover, most millimeter-wavelength observations show less limb brightening than the homogeneous models predict (Shibasaki et al. 2011). Attempts to reconcile models with millimeter-wavelength observations invoke absorbing features such as chromospheric spicules (e.g., Lantos & Kundu 1972; Selhorst et al. 2005). This approximation could be valid for the TR and the corona where spicules are cooler than the ambient medium but not necessarily so for the chromosphere (e.g., Tsiropoula et al. 2012).

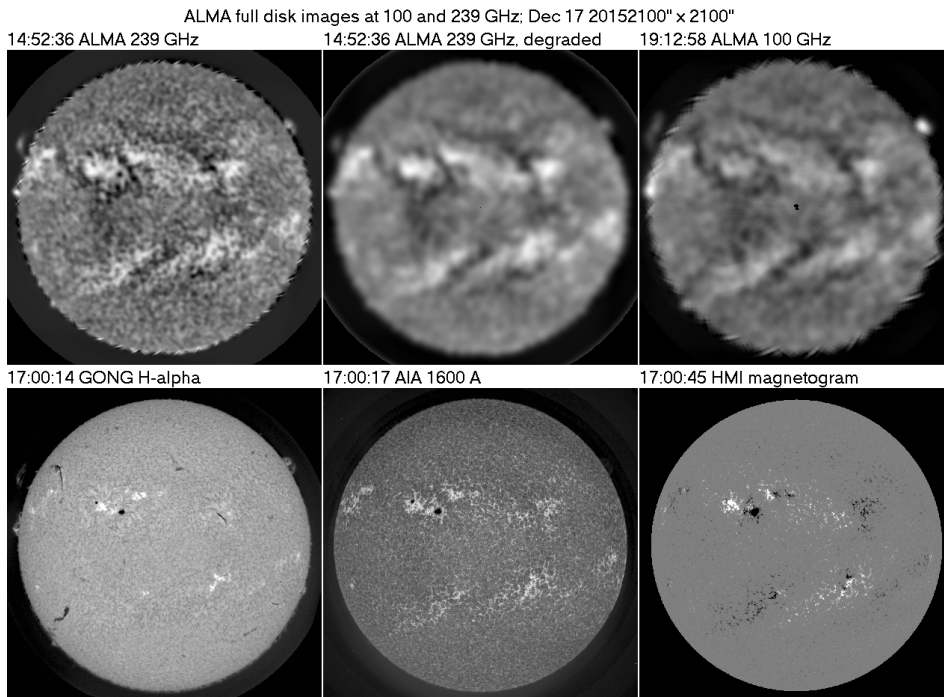


**Fig. 1.** ALMA full disk images on December 17, 2015, compared with images at other wavelengths. *Top row, left to right:* ALMA image at 239 GHz; the same, degraded to the 100 GHz resolution; and ALMA image at 100 GHz. *Bottom row:* H $\alpha$  from the GONG network; 1600 Å image from AIA/SDO; and magnetogram from HMI/SDO. The images have been partly corrected for center-to-limb variation. ALMA images are shown with the same contrast.

In this article we use recently released full-disk data from the Atacama Large Millimeter/submillimeter Array (ALMA) at 100 and 239 GHz (3 and 1.26 mm, respectively) to study the center-to-limb variation of the emission and retrieve information on the variation of temperature with optical depth. Although these data have much lower resolution than the interferometric ALMA data, the coverage of the entire solar disk, the low noise, the accurate absolute calibration, and the great sensitivity of ALMA make these data important for our purpose. Moreover, we compare the mm- $\lambda$  disk structures with those in other wavelengths.

## 2. Observations

We analyzed data at 100 and 230 GHz obtained during solar commissioning activities on 2015 December 16, 17, 18, and 20 and released as ALMA Science Verification data in early 2017. The observations were carried out in a compact array configuration, which included twenty-two 12 m antennas and nine 7 m antennas. Single dish, fast-scanning observations from 12 m “total power” (TP) antennas covering the full solar disk were carried out simultaneously. The TP antennas observed the full solar disk (FD) within three minutes. The full width at half maximum (FWHM) of the single dish beam is about 27'' at 239 and 60'' at 100 GHz, the sampling step 3 and 6'', respectively, and the field of view 2400'' at both frequencies. The procedure for solar observations with ALMA is described in White et al. (2017).

The data set comprises of two FD images on December 16 and four on December 17 at 100 GHz, and one image per day on December 17, 18, and 20 at 239 GHz. Figure 1 shows ALMA full disk images at both frequencies for December 17, 2015. To facilitate the comparison between the two, we added a 239 GHz image degraded to the 100 GHz resolution. We also give H $\alpha$  and 1600 Å images and a magnetogram. The images have been partly corrected for center-to-limb variation to enhance the visibility of the disk features and show prominences at the same time. Some irregularities appear at the limb of the ALMA images, which are due to the way that the antennas scan the Sun. As the data close to the limb are not used here, these do not affect our results.

The four 100 GHz images on December 17 gave us the opportunity to check the stability of the instrument. The total flux of the Sun was remarkably stable with an rms of 0.2%. On the disk, the rms variation of the brightness temperature was not greater than 0.25% of the average, while at the limb it was  $\sim 5\%$  of the average, but this was mainly due to irregularities arising from the scanning procedure. The second image of December 16 was within 0.8% of the December 17 images, however the first image of the same day was 3.3% brighter and we preferred to ignore it in our analysis. Similarly, the three 239 GHz images on December 18–20 were stable to within 0.3%.

In the process of correcting the images by subtracting the center-to-limb variation, we found that the solar disk was slightly elliptical in shape; this has nothing to do with any pole-equator asymmetry, since the major axis of the ellipse was inclined by about 45° east of the north pole. Although the effect was very small, amounting to a variation of the disk radius with amplitude of  $\sim 0.2\%$ , we took this effect into account because it was clearly visible in the images corrected for center-to-limb variation. The origin of this effect and of the irregularities near the limb probably lies in small pointing errors during the scanning process and/or in the algorithm of image reconstruction.

## 3. Results

The structure of the ALMA images (Fig. 1) is broadly consistent with previous works (Bastian et al. 1993; Iwai & Shimojo 2015). Plage regions are the most prominent feature on the disk. The big sunspot in AR 12470, at N12W12, is well visible at 239 and barely discernible at 100 GHz. Prominences are well visible beyond the limb, but large-scale neutral lines rather than filaments are seen on the disk as darker-than-average features. The chromospheric network is well visible at 239 GHz and is very similar to the AIA 1600 and 304 Å images (Fig. 2), but the correlation is slightly better with 1600 Å. This is a strong indication that the emission is formed at about the same level. Bogod et al. (2015) found that cm- $\lambda$  structures correlate best

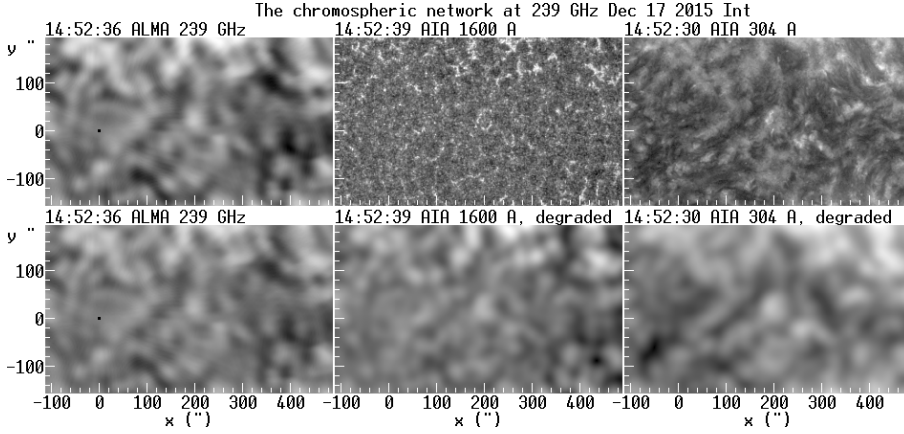


**Fig. 2.** Images of the chromospheric network near disk center from the ALMA FD image of December 17, 2015 at 239 GHz, together with 1600 Å and 304 Å AIA images. In the *bottom* row the AIA images were degraded to the ALMA resolution.

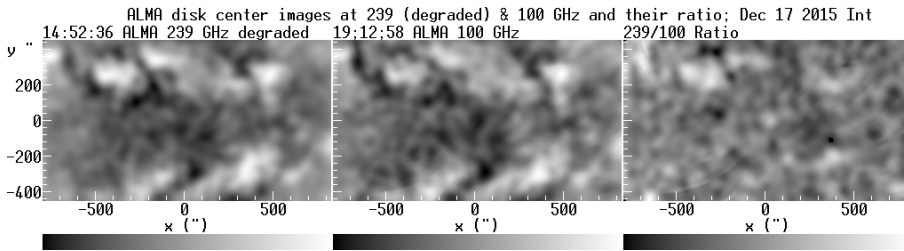


**Fig. 3.** Degraded 239 image, the 100 GHz image, and their ratio. Values range from 6000 to 7380 K, 6860 to 8380 K and 0.83 to 0.93, respectively.

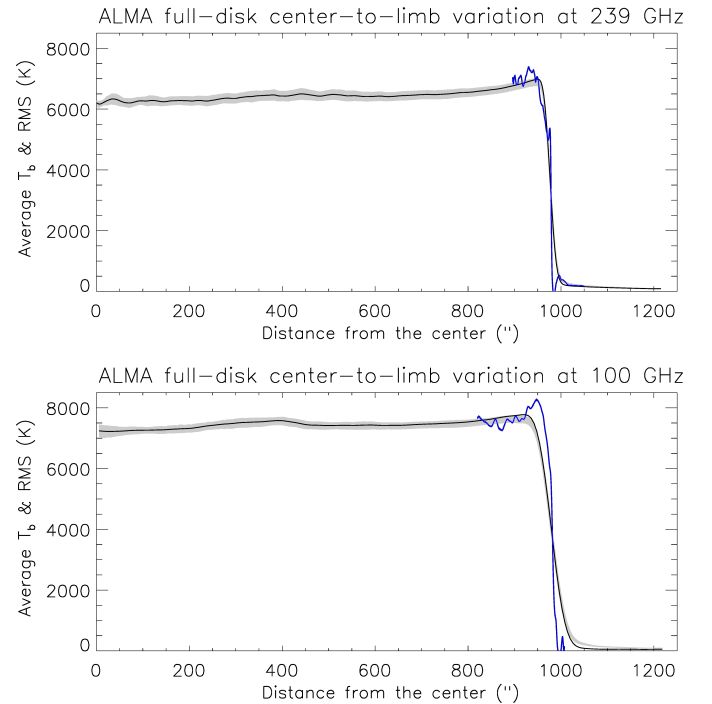
with the 304 Å AIA band, which is formed higher in the low transition region.

Figure 3 shows the 239/100 GHz intensity ratio; it ranges from 0.83 to 0.93, corresponding to a spectral index from  $-0.21$  to  $-0.083$ . The average value of the ratio is 0.87 with a dispersion of 0.01. The ratio is higher for the active region plage, which has a flat spectrum, but not for the faculae in the south hemisphere. The dark lanes between the faculae are indistinguishable in the ratio image. Also, the network appears more diffuse in the degraded 239 GHz image than at 100 GHz; since this is the opposite of what we expected because the 239 GHz radiation is formed lower in the atmosphere, we suspect that the antenna beam at 100 GHz is narrower than estimated.

For the computation of the center-to-limb variation (CLV), we calculated the brightness temperature,  $T_b$ , as a function of distance from the disk center,  $r$ , after masking out the pixels that were either too bright (plage) or too dark (sunspot and filament channels); the results are shown in Fig. 4. The degrading effect of the antenna beam did not allow us to produce separate CLV curves for the network and cell interior; still a lower limit of their difference can be estimated from the intensity rms at each point, which also appears in Fig. 4.

In order to check how close to the limb our FD values are reliable, we computed CLV curves from two high resolution ALMA images that were included in the data set: one near the east limb on December 16 at 100 GHz and one at the south pole on December 20 at 239 GHz. We noticed that the flux of these images was higher than that of the FD, by 4% for 239 and 15% for 100 GHz, apparently due to imperfect matching of the FD and high resolution flux. The high resolution CLV curves, corrected for this effect, are overplotted in Fig. 4. The comparison with the FD curves shows that we are safe in using measurements up to  $r \approx 960''$  with a photospheric radius of  $975.2''$ .

The CLV curves of Fig. 4 show that  $T_b$  does not drop to zero beyond the limb; at  $r = 1200''$  ( $160 \times 10^3$  km above the photospheric limb) it has a value of 100 K at 239 and 93 K at 100 GHz. This effect could be due to (a) a coronal component; (b) the atmospheric background; or (c) extended wings in the



**Fig. 4.** Center-to-limb variation (CLV) for 239 and 100 GHz. The gray band shows the measured values  $\pm$  the corresponding rms. The superposed blue curves near the limb are from high resolution ALMA images. Curves in black show the CLV after correction for diffuse light.

antenna response (diffuse light). We can exclude the first possibility because the coronal contribution is very small; indeed, Alissandrakis et al. (2013), using differential emission measure derived from AIA, estimated the coronal contribution just beyond the limb to  $\sim 8000$  K at  $\lambda = 5.2$  cm (see their Fig. 9), which leads to  $T_b \approx 25$  K at 100 GHz and 5 K at 239 GHz. The second possibility is rather unlikely owing to the careful ALMA calibration. We thus consider that the effect is due to the antenna

response and thus it has a small influence on  $T_b$  far from the limb.

In order to improve the measurements closer to the limb, we performed a correction for diffuse light as follows: we first estimated the extended wings of the antenna response by computing the derivative of the CLV curve near the limb; this was better fitted with a Voigt function rather than with a Gaussian and we attributed the extended wings of the Voigt function to the diffuse light and the Gaussian core to the combination of the antenna core and the actual limb profile. For the correction, we deconvolved with the Voigt function and reconvolved with the Gaussian core. The result is shown by the black curves in Fig. 4. The correction did not change the slope of the CLV curve at the limb, while it slightly increased  $T_b$  before the limb and reduced the diffuse light component beyond.

Both CLV curves are very flat, apart from some irregularities from remaining structures with a slow but statistically significant increase toward the limb, as noted by Bastian et al. (1993), at 353 GHz. The average brightness temperature at a distance smaller than  $30''$  from the center of the disk is 6180 and 7250 K at 239 and 100 GHz, respectively, with dispersions of 100 and 170 K. These fall within the “cluster” of values compiled by Loukitcheva et al. (2004) for this spectral range; we add that Iwai et al. (2017) measured  $7700 \pm 310$  K at 115 GHz with the Nobeyama 45 m telescope. The inflection point of the CLV curve is at  $976.7 \pm 2.5''$  and  $979.8 \pm 4.5''$  for 239 and 100 GHz, respectively, which is 1000 and 3300 km above the limb; reduced to 1 AU, the solar radio radius is 961.1 and 964.1'' at 239 and 100 GHz, respectively. As expected, these values are lower than those reported by Selhorst et al. (2011) at 17 GHz for the same phase of the solar cycle, which was  $\sim 975''$ .

#### 4. Inversion of the center-to-limb curve

In principle, the variation of the electron temperature with optical depth,  $T_e(\tau)$ , can be obtained by inversion of the formal solution of the transfer equation for radio wavelengths

$$T_b(\mu) = \int_0^\infty T_e(\tau) e^{-\tau/\mu} d\frac{\tau}{\mu}, \quad (1)$$

where  $T_b$  is the brightness temperature,  $\mu = \cos \theta$  and  $\theta = \sin^{-1}(r/R_\odot)$ .

In order to extend the range of  $\mu$  and determine a single set of coefficients for all frequencies, we reduced all data to a common reference frequency,  $f_{\text{ref}}$ , using the fact that both the free-free and the  $\text{H}^-$  absorption coefficients are proportional to  $f^{-2}$ . Hence a measurement at a frequency  $f$  is remapped to

$$T_b(\mu(f/f_{\text{ref}})^2, f_{\text{ref}}) = T_b(\mu, f). \quad (2)$$

Moreover, we included the measurements of Bastian et al. (1993) at 353 GHz (0.85 mm) in our data set.

A first estimate of  $T_e$  is provided by the Eddington-Barbier (E-B) relation,  $T_e(\tau) \simeq T_{b,\mu=\tau}$ . The result is shown in Fig. 5, as a function of the logarithm of the optical depth at 100 MHz. In the same figure we plotted  $T_e(\tau)$  curves computed from standard atmospheric models, taking into account both the free-free (Zheleznyakov 1970) and  $\text{H}^-$  (Stallcop 1974) absorption.

Our E-B solution practically coincides with FAL93 Model C (average quiet Sun). However, E-B is just a first order approximation. For a more exact computation we preferred to assume a particular form for  $T_e(\tau)$ , which is a more stable procedure than a direct numerical inversion. For a logarithmic dependence of  $T_e$

on  $\tau$ , suggested by both the E-B solution and the form of the model curves,

$$T_e(\tau) = a_1 + a_2 \ln \tau, \quad (3)$$

the brightness temperature is from Eq. (1)

$$T_b(\mu) = a_1 + a_2(\ln \mu - \gamma), \quad (4)$$

where  $\gamma$  is the Euler constant. The coefficients  $a_1$  and  $a_2$  can be determined by least squares fit of the observations.

For the least squares fit we used ALMA measurements up to  $\theta \simeq 70^\circ$  to avoid regions affected by the beam near the limb and ignored small-scale irregularities. The fit was very good, with an rms of residuals of  $\sim 60$  K, while the addition of a quadratic term in Eq. (3) did not change appreciably either the data fit or the inversion results, which shows that the solution is stable. Contrary to that, a power series expansion of  $T_e(\tau)$  required at least six terms to give a good data fit and, moreover, it gave an oscillatory (hence unphysical) inversion result that did not converge even when 10 terms were retained in the expansion. This justifies further our choice of logarithmic dependence of  $T_e$  on  $\tau$ .

Our inversion results are presented in Fig. 5. In addition to the global inversion, we also performed inversions for individual frequency bands. The global inversion gave a slope of  $a_2 = -608$  K. Inversions for individual wavelength bands are very similar to the global with slopes of  $-608$ ,  $-519$ , and  $-818$  K at 100, 239, and 343 GHz, respectively.

A first remark is that the inversion values are about 350 K below the E-B solution,  $T_{\text{EB}}$ . This is because the linear expansion of  $T_e$  used in this approximation is not accurate enough; adding a quadratic term with the second derivative,  $T''_{e,\tau=\mu}$ , to the Taylor expansion of  $T_e(\tau)$  around  $\tau = \mu$ , we get

$$T_e(\tau) \simeq T_{e,\tau=\mu} + (\tau - \mu)T'_{e,\tau=\mu} + \frac{1}{2}(\tau - \mu)^2 T''_{e,\tau=\mu} \quad (5)$$

from which, applying Eq. (1), we obtain

$$T_b(\mu) \simeq T_{e,\tau=\mu} + \frac{1}{2}\mu^2 T''_{e,\tau=\mu} = T_{e,\tau=\mu} - \frac{1}{2}a_2, \quad (6)$$

where, in the last step,  $T''_{e,\tau=\mu}$  was computed from Eq. (3). From this equation we obtain for the difference between the E-B solution and the 2nd order expansion

$$T_{\text{EB}} - T_{e,\tau=\mu} \simeq -\frac{1}{2}a_2, \quad (7)$$

which evaluates to 304 K for the value of  $a_2$  given above and is very close to the difference between the E-B solution and our inversion.

Compared to the model predictions, our values are closer to the FAL93 model C (average quiet Sun),  $\sim 5\%$  lower; they are rather far from models A (cell interior) and F (network). The model of Avrett & Loeser (2008) predicts too flat a chromosphere to be compatible with our measurements.

#### 5. Summary and conclusions

Our study of the first ALMA full-disk images at 239 and 100 MHz showed that their morphology is very similar to that of AIA 1600 Å images. Plages, faculae, and the chromospheric network are the most prominent features on the disk. We see prominences beyond the limb and dark lanes on the disk at the location of large-scale neutral lines. Plage regions stand out clearly in the 239/100 GHz intensity ratio, while faculae and filament lanes

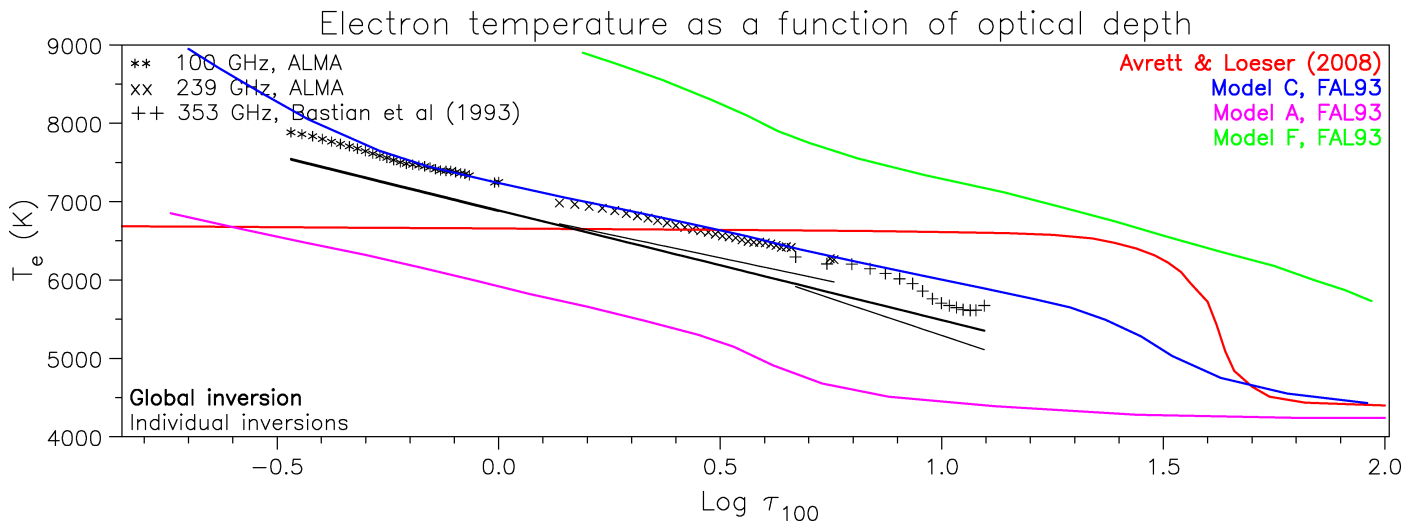


**Fig. 5.** Electron temperature as a function of the optical depth at 100 GHz. The thick black line is the result of our inversion of the CLV curves of Fig. 4, together with the data of Bastian et al. (1993). Thin black lines are inversions of individual wavelength bands. The symbols denote the Eddington-Barbier solution of the transfer equation. The full lines in color were computed from the models of Fontenla et al. (1993; FAL93) and Avrett & Loeser (2008).

do not. The brightness temperature at the center of the disk is 6180 and 7250 K at 239 and 100 GHz, respectively, with dispersions of 100 and 170 K. The solar disk radius, reduced to 1 AU, is  $961.1 \pm 2.5$  and  $964.1 \pm 4.5''$ .

Rather than comparing our center-to-limb measurements of the brightness with model predictions, we inverted these and obtained direct information on the variation of the electron temperature with the optical depth. Compared to spectral observations at discrete frequencies, CLV data have the advantage of covering a wider range of optical depths; the fact that they are obtained with the same instrument and at about the same time, gives them the additional advantage of homogeneity of observing conditions and phase in the solar cycle.

Our global inversion, combining the two ALMA frequencies and the data of Bastian et al. (1993) at 353 GHz, samples a  $\tau_{100}$  range between 0.34 and 12. It is broadly consistent with a linear variation of electron temperature with the logarithm of the optical depth in the chromosphere, where the observed radiation is formed. Although we are  $\sim 5\%$  below the model C of FAL93, we do not confirm previous results (see Shibasaki et al. 2011, and references therein) that the observations are better fitted with the cell interior model A. A potentially interesting aspect is that we do not reproduce the increased gradient of  $T_b$  predicted by model C below  $\log(\tau_{100}) = -0.3$  (Fig. 5) and this may indicate that the temperature rise occurs higher than predicted by the model. However, our results in this  $\tau$  range rely on 100 GHz measurements 30 to  $55''$  from the limb, which may have been affected by the  $60''$  antenna beam.

It is difficult to establish a height scale on the basis of mm- $\lambda$  observations alone. Resorting to model C of FAL93, the height corresponding to our range of optical depth is from 980 to 1990 km. The accurate determination of the position of the limb with high resolution ALMA observations will help to deduce empirical information on the height of formation of the mm- $\lambda$  emission. High resolution ALMA observations will also allow us to measure the ratio of network to cell intensity and feed this information to multi-component models, something that could

not be done with the present, low resolution, full-disk data. Last but not least, as more ALMA frequency bands become available for solar observations, the range of heights sampled will extend from the upper photosphere to the low transition region, providing a unique tool for the study of solar atmospheric structure.

*Acknowledgements.* This paper makes use of the following ALMA data: ADS/JAO.ALMA#2011.0.00020.SV. ALMA is a partnership of ESO (representing its member states), NSF (USA), and NINS (Japan), together with NRC (Canada) and NSC and ASIAA (Taiwan), and KASI (Republic of Korea), in cooperation with the Republic of Chile. The Joint ALMA Observatory is operated by ESO, AUI/NRAO, and NAOJ. The authors gratefully acknowledge use of data from the AIA and HMI (SDO) as well as the GONG databases.

## References

- Alissandrakis, C. E., Kochanov, A. A., Patsourakos, S., et al. 2013, *PASJ*, **65**, S8  
 Avrett, E. H., & Loeser, R. 2008, *ApJS*, **175**, 229  
 Bastian, T. S., Ewell, M. W., & Zirin, H. 1993, *ApJ*, **415**, 364  
 Belkora, L., Hurford, G. J., Gary, D. E., et al. 1992, *ApJ*, **400**, 692  
 Bogod, V. M., Alissandrakis, C. E., Kaltman, T. I., & Tokhchukova, S. K. 2015, *Sol. Phys.*, **290**, 7  
 Ewell, M. W., Jr., Zirin, H., Jensen, J. B., et al. 1993, *ApJ*, **403**, 426  
 Fontenla, J. M., Avrett, E. H., & Loeser, R. 1993, *ApJ*, **406**, 319  
 Irirajiri, Y., Takano, T., Nakajima, H., et al. 1995, *Sol. Phys.*, **156**, 363  
 Iwai, K., & Shimojo, M. 2015, *ApJ*, **804**, 48  
 Iwai, K., Shimojo, M., Asayama, S., et al. 2017, *Sol. Phys.*, **292**, 22  
 Landi, E., & Chiuderi Drago, F. 2003, *ApJ*, **589**, 1054  
 Lantos, P., & Kundu, M. R. 1972, *A&A*, **21**, 119  
 Lindsey, C., Kopp, G., Clark, T. A., et al. 1995, *ApJ*, **453**, 511  
 Loukitcheva, M., Solanki, S. K., Carlsson, M., et al. 2004, *A&A*, **419**, 747  
 Selhorst, C. L., Silva, A. V. R., & Costa, J. E. R. 2005, *A&A*, **433**, 365  
 Selhorst, C. L., Giménez de Castro, C. G., Válio, A., Costa, J. E. R., & Shibasaki, K. 2011, *ApJ*, **734**, 64  
 Shibasaki, K., Alissandrakis, C. E., & Pohjolainen, S. 2011, *Sol. Phys.*, **273**, 309  
 Stallcop, J. R. 1974, *ApJ*, **187**, 179  
 Tsiropoulou, G., Tziotziou, K., Kontogiannis, I., et al. 2012, *Space Sci. Rev.*, **169**, 181  
 Wedemeyer, S., Bastian, T., Brajša, R., et al. 2016, *Space Sci. Rev.*, **200**, 1  
 White, S. M., Iwai, K., Phillips, N. M., et al. 2017, *Sol. Phys.*, **292**, 88  
 Zheleznyakov, V. V. 1970, *Radio Emission of the Sun and Planets* (Oxford: Pergamon Press)